Relative tsunami hazard from segments of Cascadia subduction zone for M_w 7.5-9.2 earthquakes

Amir Salaree[1] (salaree@umich.edu)

Yihe Huang[1] (yiheh@umich.edu)

Marlon Ramos[1] (ramosmd@umich.edu)

Seth Stein[2] (seth@earth.northwestern.edu)

1. *Department of Earth and Environmental Sciences, University of Michigan*

2. *Department of Earth and Planetary Sciences, and Institute for Policy Research, Northwestern University*

April 7, 2021

for submission to

Geophysical Research Letters

24

Abstract

Tsunamis from earthquakes of various magnitudes have affected Cascadia in the past. Simulations of M_w 7.5–9.2 earthquakes constrained by earthquake rupture physics and geodetic locking models show that $M_w \geq 8.5$ events initiating in the middle segments of the subduction zone can create coastal tsunami amplitudes comparable to those from the largest expected event. The simulations reveal that the concave coastline geometry of the Pacific Northwest coastline focuses tsunami energy between latitudes 44°-45° in Oregon. The possible coastal tsunami amplitudes are largely insensitive to the choice of slip model for a given magnitude. These results are useful for identifying the most hazardous segments of the subduction zone and demonstrate that a worst-case rupture scenario does not uniquely yield the worst-case tsunami scenario at a given location.

Plain Language Summary

Offshore earthquakes along the Pacific Northwest coast of the U.S. and Canada (Cascadia) can have magnitudes as high as 9.2, as was probably the case for an earthquake in the year 1700 CE that resulted in a large tsunami in Cascadia and across the Pacific Ocean. To learn more about the future tsunami hazard in the region, we design computer models of tsunamis from a wide range of earthquake scenarios. We find that almost regardless of the earthquake source details, events larger than magnitude 8.5 near the coast of Oregon can create large and widespread tsunamis along the US west coast. These are consequences of the geometry of offshore earthquake faulting and the concave shape of coastline in the region.

Key Points:

- A M_w=8.5 event in central Cascadia (Oregon) can create coastal tsunami amplitudes comparable to those from the largest possible event.
- The concave coastline contributes to larger coastal tsunami amplitudes in central Cascadia.
- The choice of slip model does not significantly affect the distribution of coastal tsunami amplitudes in Cascadia.

1. Introduction

Coupling between the subducting Juan de Fuca plate and the overriding North America at the shallow-dipping Cascadia subduction zone [Crosson & Ownes, 1987] is expected to cause future large earthquakes and tsunamis. Previous studies [Atwater, 1987; Satake *et al*, 2003; Goldfinger *et al*, 2017] show that the ~1100-km plate boundary extending from British Columbia to northern California has generated large tsunamis in the past. The tsunami from the most recent great Cascadia earthquake or sequence of events, with an inferred total magnitude of 9 [Melgar, 2021], devastated the American and Japanese coasts on 26 January 1700 [Satake *et al*, 1996] as shown by Native American oral traditions [Heaton & Snavely, 1985] and detailed Japanese written accounts [Atwater *et al*, 2015]. Geological and paleoseismic evidence also indicates earlier prehistoric tsunamigenic events [Atwater *et al*, 1991; Darienzo & Peterson, 1995; Peters *et al*, 2003; Goldfinger *et al*, 2012].

A major challenge to modeling future Cascadia tsunami hazards is the large uncertainty in recurrence interval. Very large Cascadia events seem to occur on average every 400-500 years, and smaller events ($M_w \lesssim 8.7$) are thought to occur every ~200 years. However, the uncertainties in these measurements are sometimes on the same order of magnitude as the measurements themselves [e.g., Kelsey *et al*, 2005; Goldfinger *et al*, 2012]. Hence, it is challenging to assess tsunami hazards from different rupture segments along the coast [e.g., González *et al*, 2009]. Along-strike segmentation in the subduction zone is usually associated with variabilities in outer wedge morphology and structure [Watt & Brothers, 2021]. Another source of uncertainty is the limited constraints on the location and size of slipping segments of the subduction zone, and thus

75 the magnitude of future earthquakes, due to the absence of well-constrained information on the
76 lateral extent of past ruptures [e.g., Witter *et al*, 2011; Goldfinger *et al*, 2017].

77 Tsunami hazard in Cascadia has been modeled as a function of various recurrence
78 intervals and earthquake magnitudes, yielding results expressed as hazard curves and inundation
79 maps for sites along the coast [e.g., Thio & Somerville, 2009; Thio *et al*, 2010; Priest *et al*, 2013;
80 Park *et al*, 2017]. Such studies, which are also conducted for other, better-documented subduction
81 zones [e.g., Satake, 2015] are useful in planning response to tsunamis [Lindell & Prater, 2010].
82 However, they often do not distinguish between hazards due to rupture from various sections of
83 the subduction zone.

84 Our study aims to identify the most hazardous segments of the Cascadia subduction zone
85 by considering a range of earthquake scenarios and resulting tsunamis. We use a set of rupture
86 scenarios derived by scaling the slip distribution prescribed by locking models as initial
87 conditions to simulate Cascadia tsunamis. We then compare our tsunami simulation results to
88 those based on dynamic ruptures as well as perturbed versions of these rupture scenarios to
89 identify the contribution of various portions of the subduction zone. Finally, we use simple
90 numerical experiments with synthetic bathymetry to investigate the contribution of Cascadia
91 coastal morphology to the distribution of tsunami amplitudes. The result helps us better
92 understand the contribution of source and coastal components to Cascadia tsunamis.

93

94 # 2. Methods
95

2.1 Rupture Model & Scaling of Slip

Our earthquake simulations are based on locking models that estimate the slip deficit on the plate interface needed to match geodetic observations [Li *et al*, 2018]. If all the deficit were released in a single earthquake, the model would yield the maximum possible slip and the largest earthquake. However the next event may not release all the accumulated stress. We use the Gamma locking model [Schmalzle *et al*, 2014] to represent high levels of slip-deficit extending to the trench (Fig. 1d). In contrast with models with more uniform slip distributions, releasing the accumulated slip mostly confined near the trench would result in pulse-like, relatively short-period tsunami fronts. Due to very large seafloor uplift in the immediate vicinity of the trench, such a model results in relatively larger coastal tsunami waves, especially in the near-field. By assuming an average recurrence interval T_r for stress release, as inferred from offshore turbidite deposits [Goldfinger *et al*, 2012, 2017], we convert the slip rate deficit in the locking model to slip. An average value of T_r, i.e., 320 years [Goldfinger *et al*, 2017] results in a maximum slip amplitude of ~20 m along the trench in northern Cascadia.

We discretize the rupture into 25×25 km blocks (Fig. 1), each of which is considered as a pure double-couple source with the dip of the slab, the azimuth of the trench, and a slip angle of 90°. We then calculate a surface deformation field [Mansinha & Smylie, 1972] using the average slip value within the block. Because smaller earthquakes require less accumulated stress over

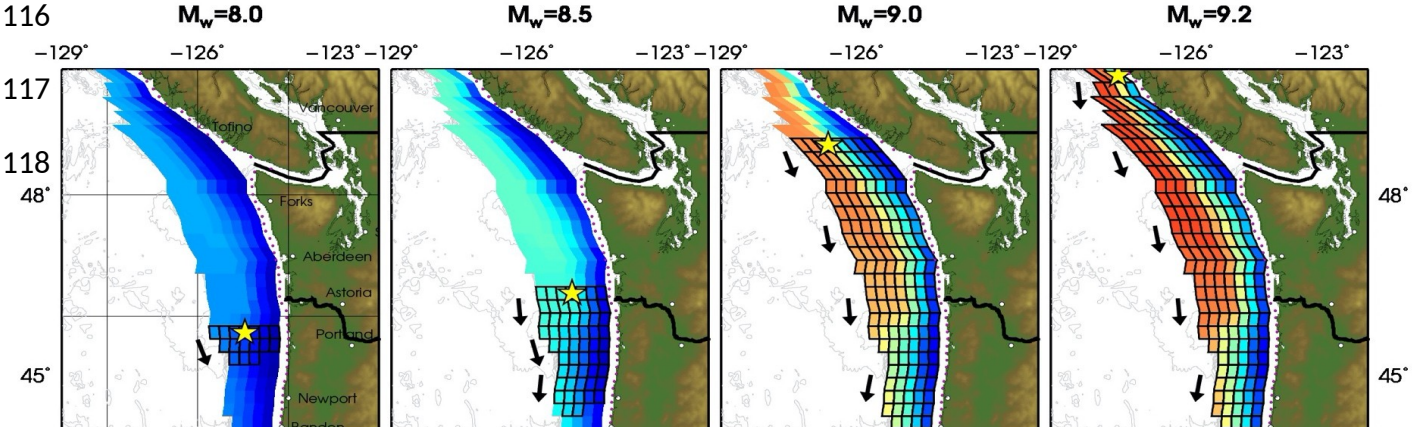

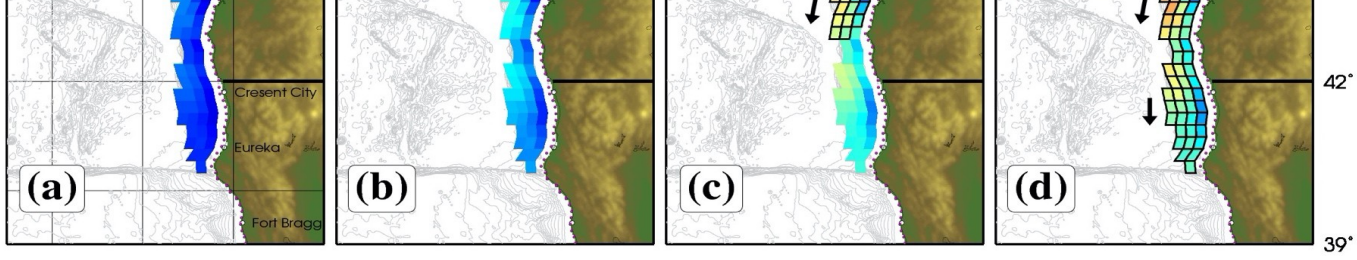

Figure 1. Scaled dislocation fields at the ocean floor calculated from the locking model for (a) M_w=8.0, (b) M_w=8.5, (c) M_w=9.0, and (d) M_w=9.2. Meshes show sample north-south rupture scenarios s. Black arrows denote the direction of rupture propagation from the hypocenters marked by yellow stars.

times er, the main trends of coastal amplitude distribution are not affected by the choice of scaling equations (see supplementary material).

We construct a field of ocean floor dislocations for six magnitudes: M_w=7.5, 8.0, 8.5, 9.0, 9.1 and 9.2 (Fig. 1). The two largest magnitudes are selected to obtain better resolution of the tsunami hazard for the potentially largest events. The hypocenter is not positioned at the trench to guarantee that the rupture nucleates between the surface and the base of the seismogenic zone near ~30 km depth [Wang & Tréhu, 2016]. For each magnitude we start rupture scenarios at the

138 northernmost block for the chosen geometry and propagate the rupture southward until it is large
139 enough to yield the desired magnitude. Rupture propagates along strike and dip with speeds
140 between 2 - 3 km/s before reaching the bottom of the seismogenic zone, mimicking an elliptical
141 rupture. This process is then repeated by moving the hypocenter one block south, resulting in a
142 new scenario. This approach leads to 118 rupture scenarios. In our model, ruptures of M>8.5
143 earthquakes primarily propagate along strike because the down-dip rupture extent saturates,
144 resulting an elongated rupture area (Fig. 1). This process yields a frequency-magnitude
145 distribution similar to the Gutenberg-Richter distribution due to the constraints resulting from
146 rupture areas on the overall seismic moment [Stein & Wysession, 2003; Fig. S2]. Our arbitrary
147 choice of rupture directivity (north to south) has little effect because of the proximity of the
148 coastlines to the trench (~150 km) and the large dominant wavelength of the tsunami
149 [Rabinovich, 1997] prevent the rupture duration from significantly affecting the coastal tsunami
150 amplitudes. Numerical experiments with various modes of rupture in flat oceans and near
151 coastlines of different morphologies reveal that the contribution of rupture directivity is not
152 significant in the near field (Fig. S3), as also shown by Williamson *et al* [2019].

153

154 ## 2.2 Tsunami Simulation Method

155 We simulate tsunamis from each scenario using the MOST algorithm [Titov *et al*, 2016]
156 that solves the fully nonlinear version of the shallow water approximation of the Navier-Stokes
157 equation. MOST has been extensively validated through comparisons with laboratory and field
158 data using standard international protocols [Synolakis *et al*, 2008]. Simulations are performed for
159 4.5 hr time windows, allowing the tsunami to propagate along the entire coast. These simulations

160 use 0.5 s time steps to satisfy the stability-resolution requirement [Courant *et al*, 1928]. Wave
161 height calculations are truncated at a depth of 30 m along the coastlines (typically at a distance of
162 1-4 km) to avoid nonlinear shoaling effects, especially in the presence of large offshore
163 deformation values. Therefore, no run-up values are calculated. Although run-up typically
164 increases the tsunami hazard for generally linear coastal bathymetry and in the absence of bays,
165 the distribution of coastal amplitudes (at shallow depth) will almost match that of run-up [Plafker,
166 1997]. We calculate time histories of tsunami amplitudes at 100 virtual gauges along the coastline
167 at a depth of ~35 m and one gauge at the entrance of the Strait of Juan de Fuca, north of Fork. We
168 use GEBCO bathymetry interpolated to a spatial resolution of 18 arc-seconds to ensure enough
169 (~20) grid points per wavelength [Shuto *et al*, 1986].

170 MOST was developed to model static sources and cannot be directly applied to kinematic
171 ruptures [Titov & Synolakis, 1998]. Hence, we apply it to the discretized rupture blocks each of
172 which happens at time t_i after the origin time. For each block, calculations are terminated after a
173 duration Δt and the outputs are fed into MOST as initial conditions for the next block. The
174 process continues until rupture ends after which the problem turns into a regular tsunami
175 propagation. Although this approach introduces discontinuities in both water surface elevation
176 and velocity, it produces results comparable to those from fully kinematic algorithms such as
177 GeoClaw [Berger *et al*, 2011, González *et al*, 2011] that have been verified for Cascadia [Melgar
178 *et al*, 2016]. The discrepancy between our results and those from the previous studies is largely
179 due to the scaling equations. As discussed earlier (Fig. S1) Geller's [1976] scaling equations
180 predict larger slip for a given rupture. While kinematic rupture properties do not significantly
181 affect near-field tsunami propagation, we consider kinematic ruptures for a more comprehensive
182 view of tsunami behaviors.

3. Cascadia Earthquake and Tsunami Scenarios

3.1 Tsunami Simulation Results

We analyze the tsunami hazard for our rupture scenarios (Fig. 1) by simulating the resulting tsunamis. Our magnitude range of M_w=7.5–9.2 accommodates both the largest expected rupture and the smallest rupture with noticeable ocean floor deformation (~1m). Note that the smallest rupture does not necessarily reach the ocean floor. Tsunami simulations for the rupture scenarios are shown in Fig. 2 (also see supplementary material). We find that various earthquake magnitudes can create similar tsunami amplitudes at a given location depending on the position of the hypocenter. For example, as shown in Figs. 2b and 2c, a M_w=8.5 earthquake with a hypocenter in the south (~43°N) and a M_w=9.0 earthquake starting further north (~48°N) both produce tsunami amplitudes of ~8 m at Newport (~44.5°N). This partly reflects geometrical spreading wherein the energy flux in the propagating tsunami decreases with increasing distance. However, as seen in Fig. 2, this trend is not monotonic.

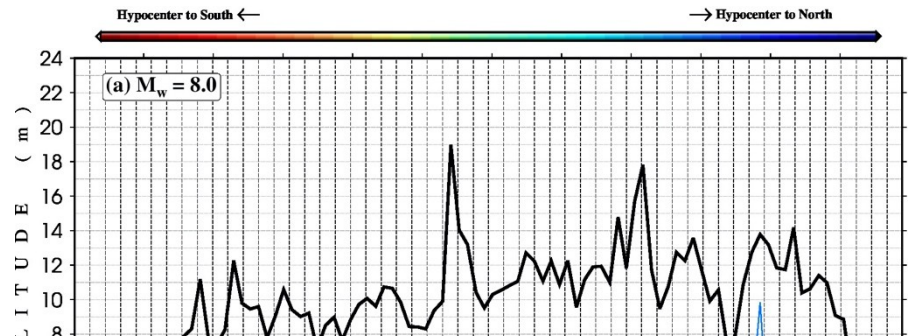

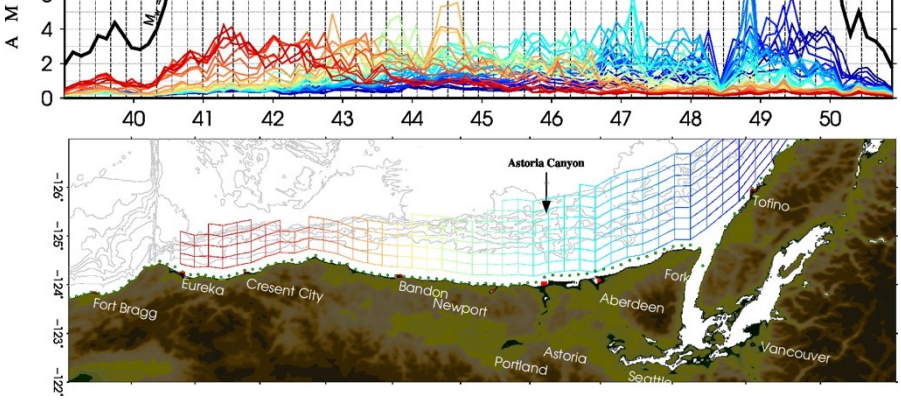
A M
0
2
4
40
41
42
43
44
45
46
47
48
49
50
Astoria Canyon
Tofino
Eureka
Cresent City
Bandon
Newport
Aberdeen
Fort Bragg
Astoria
Portland
Vancouver
Seattle
−126°
−125°
−124°
−123°
−122°

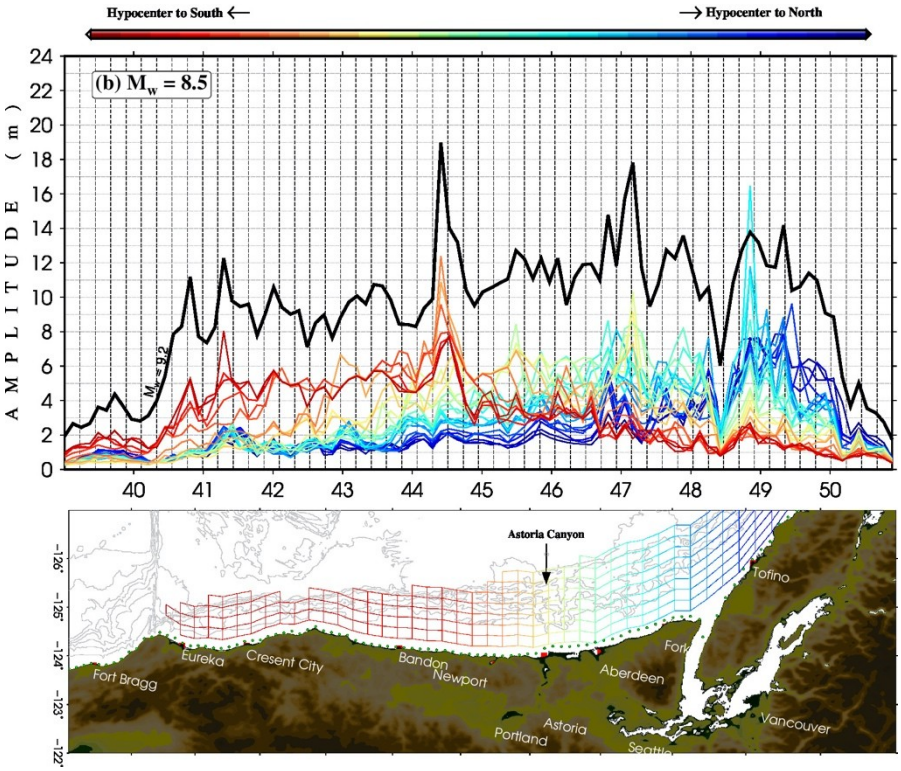
Hypocenter to South ←
→ Hypocenter to North
(b) M_w = 8.5
A M P L I T U D E (m)
0
2
4
6
8
10
12
14
16
18
20
22
24
40
41
42
43
44
45
46
47
48
49
50
M_w 9.2
Astoria Canyon
Tofino
Eureka
Cresent City
Bandon
Newport
Aberdeen
Fort Bragg
Astoria
Portland
Vancouver
Seattle
−126°
−125°
−124°
−123°
−122°

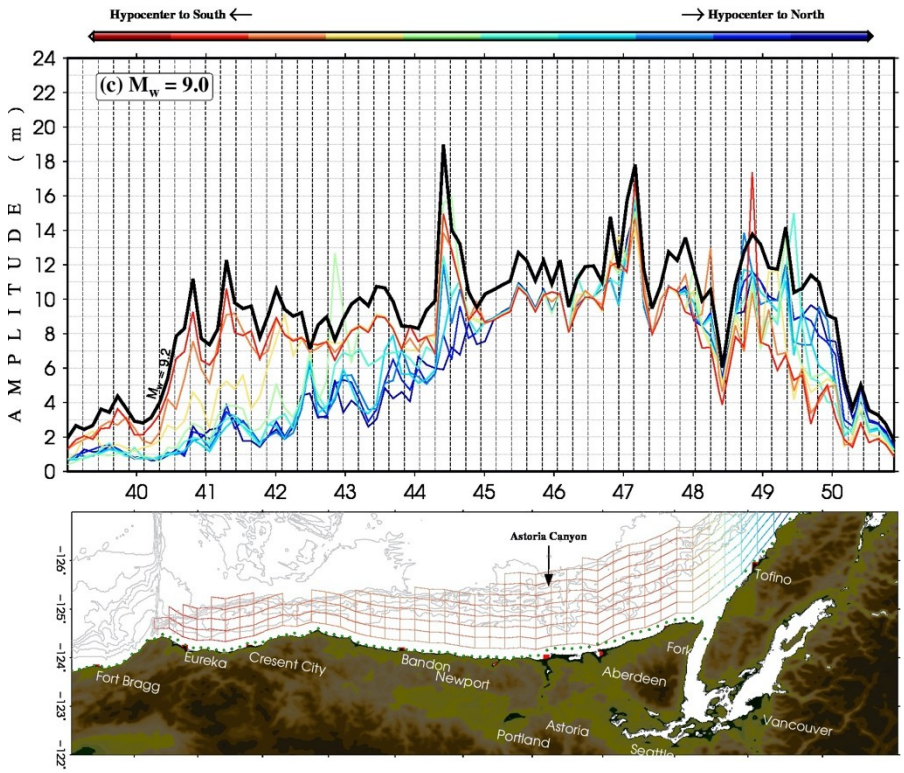
Hypocenter to South ←
→ Hypocenter to North
(c) M_w = 9.0
A M P L I T U D E (m)
0
2
4
6
8
10
12
14
16
18
20
22
24
40
41
42
43
44
45
46
47
48
49
50
M_w 9.2
Astoria Canyon
Tofino
Eureka
Cresent City
Bandon
Newport
Aberdeen
Fort Bragg
Astoria
Portland
Vancouver
Seattle
−126°
−125°
−124°
−123°
−122°

The curves are color-coded according to hypocenter latitude with hot colors in the south and cold colors in the north. Black curve shows coastal tsunami amplitudes for the M_w=9.2 event; *[Bottom]* Cascadia coastline and the rupture blocks are colored to provide a sense of hypocenter latitude. Gray contours indicate bathymetry. Large population centers are shown for reference.

3.2 Effects of Coastal Geometry

Spatial variation of near-shore tsunami amplitudes from large sources mostly reflects the influence of piecewise coastal slopes [Kânoğlu & Synolakis, 1998], because the near-shore bathymetry of Cascadia varies little with latitude (with the exception of the Astoria Canyon [Griggs & Kulm, 1970]). In fact, bathymetric profiles across all latitudes within 400 km from shoreline have a correlation coefficient of ≈0.75. Hence, in the absence of major bathymetric features the largest amplitudes occur at the latitudes with the largest earthquake slip, due to geometrical spreading and directivity [Ben-Menahem & Rosenman, 1972; Aki & Richards, 2002]. The latter causes the waves to interfere constructively in a direction perpendicular to the rupture, focusing tsunami energy onto the closest shorelines (Fig. 3).

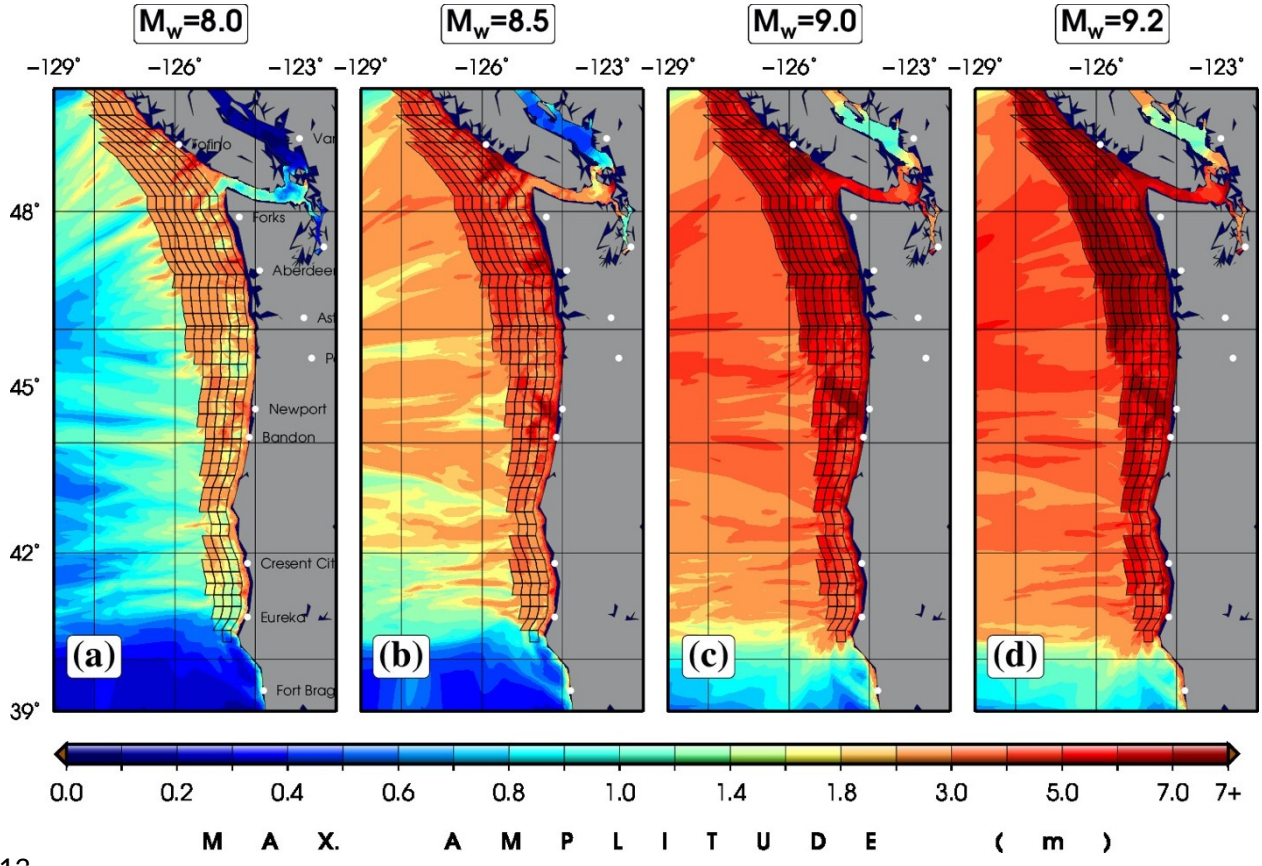

Figure 3. Cumulative maximum tsunami amplitudes for (a) M_w=8.0, (b) M_w=8.5, (c) M_w=9.0, and (d) M_w=9.2 source scenarios. Each panel shows the largest tsunami amplitudes across all rupture scenarios for a given magnitude.

224

225 The simulations reveal that in the absence of significant local bathymetric features, the
226 concave geometry of the coast between 43° - 48°N concentrates amplitudes in central Cascadia
227 (between 44° - 45°N; around Newport, Oregon) especially from ruptures in central Cascadia, in
228 agreement with edge wave theory [Munk *et al*, 1956]. We carried out numerical tsunami
229 simulations in flat oceans along a narrow, shallow continental shelves to study the effects of a
230 coastline curvature (Figs. S3 and S4) on tsunami amplitudes. These experiments show that
231 coastline concavity increases the tsunami energy in the nadir (here, mid-latitudes) by focusing the
232 energy of edge wave modes along the coast, on the continental shelf. Another amplitude peak
233 offshore, which approaches the shoreline by increasing curvature, results from the concentration
234 of tsunami reflection at the focal point of the curved shoreline. The cluster appears at half the
235 radius of coastline curvature (i.e., focal point) of coastline analogous to that predicted by
236 geometric optics for concave mirrors (see Fig. S4 in supplementary material, and the
237 supplementary video SV1).

238 Given the shoreline's large radius of curvature (~1000 km), the former effect is more
239 pronounced and can increase coastal amplitudes in central Cascadia by more than ~10%. We
240 attribute the relatively larger amplitudes near Oregon in all the scenarios (Fig. 2) to this
241 phenomenon. Although this effect makes Oregon coast almost as hazardous as northern regions
242 (near Washington), it does not violate the generalizations that smaller earthquakes create smaller
243 tsunamis, and that shorelines closer to large fault slip experience larger tsunami waves, which are
244 generally true for linear coastlines and in the absence of bays [Davies *et al*, 2018] (Figs. S3 to
245 S5).

246 Another interesting simulation result is the apparent relative immunity of northern
247 California coastlines to Cascadia tsunamis, especially from M_w<9.0 earthquakes with hypocenters
248 in the north. At first glance, this is surprising given to the region's proximity to a slip cluster near
249 the southern tip of the rupture. However, it results from both the end of rupture and the convex
250 promontory near Eureka (Fig. 2), south of where coastal amplitudes drop. Simulations suggest
251 that the coastal morphology creates and scatters free edge waves (supplementary material),
252 making the California shorelines virtually sheltered.

253 **3.3 Choice of Slip Model**

254 The distribution of potential slip from the locking model shows two main clusters (Fig.
255 1d). The larger cluster (both in area and slip magnitude) is in the north, close to British Columbia,
256 and the smaller one is around 44°N. However, the tsunami simulation results are not significantly
257 affected by the choice of slip models on a regional scale. We simulate tsunamis using a simple
258 slip model [modified from Priest *et al*, 2010] and found similar results to those from our more
259 physical model. As shown in Fig. 4a-e, the coastal amplitudes show a correlation coefficient of
260 0.8. We also used a dynamic rupture model with identical recurrence intervals, derived from a
261 Gaussian locking model [Schmalzle *et al*, 2014; Ramos *et al*, 2021]. Such models consider the
262 dynamic interaction of fault stresses and frictional strengths, and near-trench slip can be amplified
263 due to constructively interfering free-surface reflections within the accretionary wedge. The
264 resulting tsunami simulations yield a similar (correlation coefficient CC=0.8) distribution of
265 coastal amplitudes (Fig. 4j).

266 The absolute values of coastal tsunami amplitudes from these simpler models can locally
267 vary from our modeling results by up to 30%. However, the general trend of tsunami amplitudes

remains similar. In the absence of conclusive geodetic and seismic constraints on fault locking, we think our model adequately represents potential future ruptures and consider the 30% discrepancy as illustrating the uncertainty.

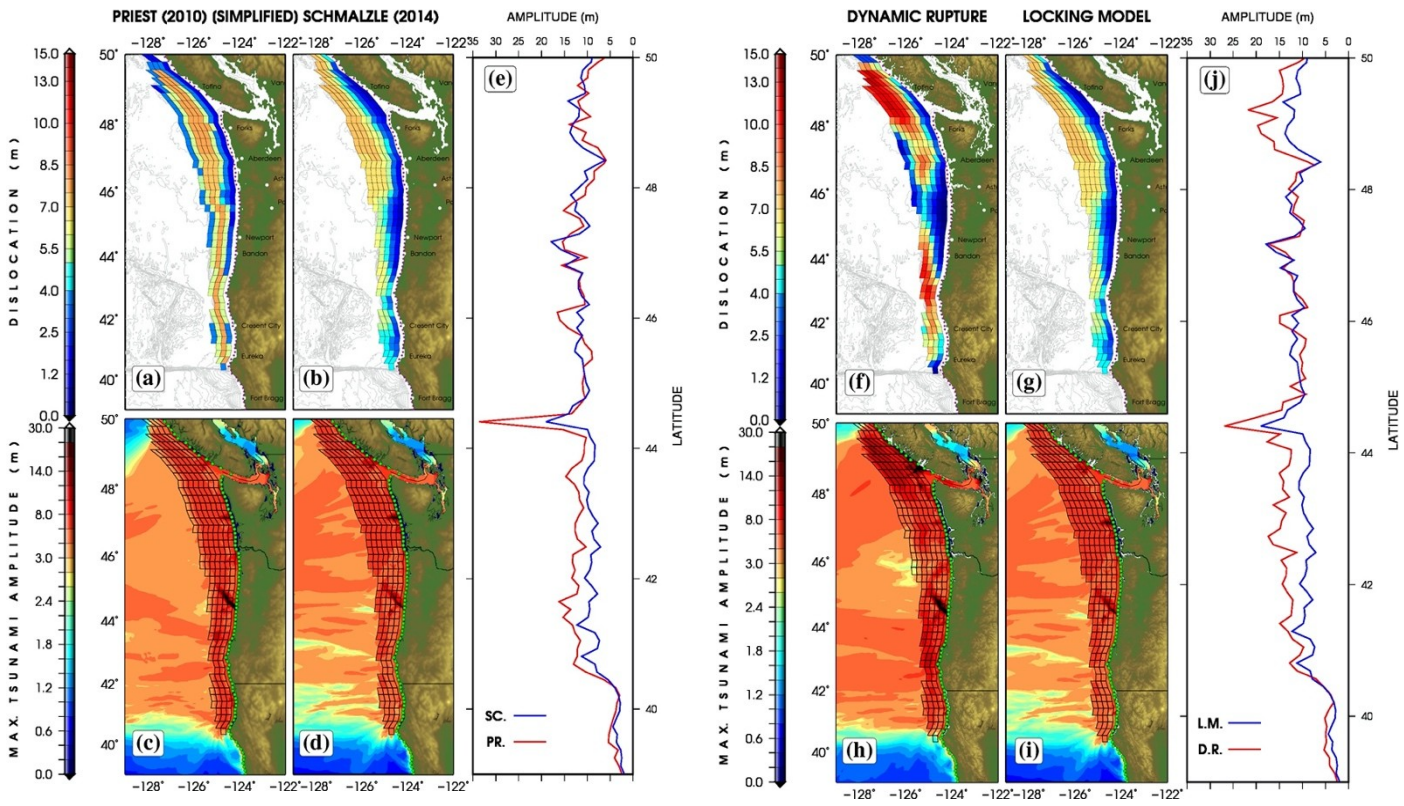

Figure 4. (a) A simplified locking model [Priest *et al*, 2010] produces similar tsunami amplitudes to those from our model shown in (b), both in the Pacific (c,d) and along the coastline (e). Also, a dynamic M_w=9.2 rupture derived from the Gaussian locking model (f) and our choice of locking model (g) result in similar tsunami amplitudes both in the Pacific (h,i) and along the coastline (j).

Simulation of the tsunami from a perturbed version of our choice of locking model (created by introducing white noise equal to 50% of the maximum to the deformation field of parent model) yields a significantly different distribution (CC=0.3) of coastal tsunami amplitudes (Fig. S6). We attribute this discrepancy to the disruption of large-scale slip clusters which changes the dominant period of the tsunami. Such smaller wavelengths significantly alter the interaction of the tsunami with the shoreline, thus resulting in a different pattern of coastal amplitudes. Otherwise, given the similar bathymetry along strike, different rupture models with comparable dimensions of slip clusters (baring an absence of large slip deficit in central Cascadia; Li *et al*, 2018) would result in similar tsunamis.

4 Discussion and Conclusions

Simulations of tsunamis from physics-based M_w=7.5-9.2 earthquake rupture scenarios show that largest and most widespread coastal tsunami amplitudes result from ruptures at or starting from mid-latitudes in central Cascadia. This result is almost independent of the choice of slip model as long as the dimensions of major slip clusters are preserved. Such ruptures, especially with M_w>8.5, can create tsunami amplitudes exceeding 50% of those from the largest expected M_w=9.2 rupture (Fig. S7a). Statistical analysis using the metric *MT* [Salaree & Okal, 2020] suggests that the near-field propagation patterns of tsunamis from M_w>8.5 events are very similar (supplementary material). This effect is important because realistic estimates of the expected loss are valuable in designing mitigation policy [Stein & Stein, 2014]. Although smaller earthquakes generate smaller tsunamis, their expected amplitudes (up to 12 m using our choice of

scaling law) are significant. Thus, smaller earthquakes that are more likely to occur in the near future may create comparable – though more localized – damage than the less frequent worst-case scenario [e.g., Priest *et al*, 2010; Thio *et al*, 2010].

We also find that the large-scale morphology of Cascadia's coastline focuses and defocuses tsunami energy. Simulations (Fig. S4 and video SV1) show that coastline curvature can increase the coastal tsunami amplitude by more than 10%. Comparison of Cascadia with other subduction zones where coastal curvature is insignificant (i.e., Chile with curvature of ~0.017) shows why such heightened tsunami amplitudes are not observed in these regions. Our simulations show that the southernmost sites (Fort Bragg, Eureka and Crescent City, Figs. 2 and 3) show almost no change in the tsunami amplitudes for events with increasing magnitude above M_w=9.0 (Fig. 2), due to the large promontory at ~42.5°N separating the concave coastline from that to the south (Fig. S5a). Examination of the along-strike tsunami amplitudes (Fig. 3) reveals that the relative differences throughout the simulation area are small (sometimes <1m) for earthquakes larger than M_w=9.0.

Our findings have implications for similar tectonic settings such as the Chile and Alaska subduction zones that have experienced large and heterogeneous megathrust ruptures. The bathymetry in these regions is also similar to Cascadia, i.e., almost uniform bathymetric slopes and large-scale geometric coastal morphology, in contrast with regions of more complex bathymetry such as Japan. Similarly, by identifying the most hazardous segments of the subduction zone, our results can be used to assist in selecting sites for DART tsunami sensors or novel technologies such as SMART cables [Howe *et al*, 2019]. This is important for near-field

316 tsunami warning because these instruments are mostly deployed on the up-dip side of trenches,
317 where the identification of the main areas contributing to the tsunami hazard is crucial.

318 Acknowledgments

319 The manuscript significantly benefited from invaluable discussions with Jean-Paul
320 Ampuero, Amanda Thomas and Kelin Wang. Some figures were drafted using the Generic
321 Mapping Tools [Wessel & Smith, 1998]. This study was supported by a National Science
322 Foundation grant (PREEVENTS geosciences directorate No. 1663769).

323 Data and materials availability

324 All bathymetry data used in the main text or the supplementary materials are available via
325 the General Bathymetric Chart of the Oceans (https://www.gebco.net). The tsunami simulation
326 code is maintained and distributed by the US National Oceanic and Atmospheric Administration
327 (https://nctr.pmel.noaa.gov/nthmp/). Rupture data and tsunami simulation results are available via
328 Deep Blue Data at https://doi.org/10.7302/xe96-3z26

329

330 References

331

332 Aki, K. & Richards, P. G., 2002. *Quantitative Seismology*, University Science Books.
333 Atwater, B. F., 1987. Evidence for great Holocene earthquakes along the outer coast of
334 Washington State, *Science*, **236**(4804), 942–944.

Atwater, B. F., Musumi-Rokkaku, S., Satake, K., Tsuji, Y., Ueda, K., & Yamaguchi, D. K., 2015. *The orphan tsunami of 1700: Japanese clues to a parent earthquake in North America*, University of Washington Press.

Atwater, B. F., Stuiver, M., & Yamaguchi, D. K., 1991. Radiocarbon test of earthquake magnitude at the Cascadia subduction zone, *Nature*, **353**(6340), 156–158.

Ben-Menahem, A. & Rosenman, M., 1972. Amplitude patterns of tsunami waves from submarine earthquakes, *Journal of Geophysical Research*, **77**(17), 3097–3128.

Berger, M. J., George, D. L., LeVeque, R. J., & Mandli, K. T., 2011. The GeoClaw software for depth-averaged flows with adaptive refinement, *Advances in Water Resources*, **34**(9), 1195–1206.

Courant, R., Friedrichs, K., & Lewy, H., 1928. Uber die partiellen Differenzengleichungen der mathematischen Physik, *Mathematische Annalen*, **100**(1), 32–74.

Crosson, R.S. and Owens, T.J., 1987. Slab geometry of the Cascadia subduction zone beneath Washington from earthquake hypocenters and teleseismic converted waves. *Geophysical Research Letters*, **14**(8), pp.824-827.

Darienzo, M. E. & Peterson, C. D., 1995. Magnitude and frequency of subduction-zone earthquakes along the northern Oregon coast in the past 3,000 years, *Oregon Geology*, **57**(1), 3–12.

Davies, G., Griffin, J., Løvholt, F., Glimsdal, S., Harbitz, C., Thio, H.K., Lorito, S., Basili, R., Selva, J., Geist, E. and Baptista, M.A., 2018. A global probabilistic tsunami hazard assessment from earthquake sources. *Geological Society, London, Special Publications*, **456**(1), pp.219-244.

Dominey-Howes, D., Dunbar, P., Varner, J., & Papathoma-K¨ohle, M., 2010. Estimating probable maximum loss from a Cascadia tsunami, *Natural hazards*, **53**(1), 43–61.

Geller, R. J., 1976. Scaling relations for earthquake source parameters and magnitudes, *Bulletin of the Seismological Society of America*, **66**(5), 1501–1523.

Goldfinger, C., Galer, S., Beeson, J., Hamilton, T., Black, B., Romsos, C., Patton, J., Nelson, C. H., Hausmann, R., & Morey, A., 2017. The importance of site selection, sediment supply, and hydrodynamics: A case study of submarine paleoseismology on the Northern Cascadia margin, Washington USA, *Marine Geology*, **384**, 4–46

Goldfinger, C., Nelson, C. H., Morey, A. E., Johnson, J. E., Patton, J. R., Karabanov, E. B., Gutierrez-Pastor, J., Eriksson, A. T., Gracia, E., Dunhill, G., et al., 2012. Turbidite event history–methods and implications for Holocene paleoseismicity of the Cascadia subduction zone, Tech. rep., *US Geological Survey*.

González, F.I., Geist, E.L., Jaffe, B., Kânoğlu, U., Mofjeld, H., Synolakis, C.E., Titov, V.V., Arcas, D., Bellomo, D., Carlton, D. and Horning, T., 2009. Probabilistic tsunami hazard assessment at seaside, Oregon, for near−and far−field seismic sources. *Journal of Geophysical Research: Oceans*, **114**(C11).

González, F.I., LeVeque, R.J., Chamberlain, P., Hirai, B., Varkovitzky, J. and George, D.L., 2011. Validation of the geoclaw model. **In:** *NTHMP MMS Tsunami Inundation Model Validation Workshop*. GeoClaw Tsunami Modeling Group.

Griggs, G. B. & Kulm, L., 1970. Sedimentation in Cascadia deep-sea channel, *Geological Society of America Bulletin*, **81**(5), 1361–1384.

Heaton, T. H. & Hartzell, S. H., 1987. Earthquake hazards on the Cascadia subduction zone, *Science*, **236**(4798), 162–168.

Heaton, T. H. & Snavely Jr, P. D., 1985. Possible tsunami along the northwestern coast of the United States inferred from Indian traditions, *Bulletin of the Seismological Society of America*, **75**(5), 1455–1460.

Howe, B.M., Arbic, B.K., Aucan, J., Barnes, C.R., Bayliff, N., Becker, N., Butler, R., Doyle, L., Elipot, S., Johnson, G.C. and Landerer, F., 2019. SMART cables for observing the global ocean: science and implementation. *Frontiers in Marine Science*, **6**, p.424.

Kânoğlu, U. and Synolakis, C.E., 1998. Long wave runup on piecewise linear topographies. Journal of Fluid Mechanics, 374, pp.1-28.

Kelsey, H.M., Nelson, A.R., Hemphill-Haley, E. and Witter, R.C., 2005. Tsunami history of an Oregon coastal lake reveals a 4600 yr record of great earthquakes on the Cascadia subduction zone. *Geological Society of America Bulletin*, **117**(7-8), pp.1009-1032.

Li, S., Wang, K., Wang, Y., Jiang, Y., & Dosso, S. E., 2018. Geodetically inferred locking state of the Cascadia megathrust based on a viscoelastic Earth model, *Journal of Geophysical Research: Solid Earth*, **123**(9), 8056–8072.

Lindell, M.K. and Prater, C.S., 2010. Tsunami preparedness on the Oregon and Washington coast: Recommendations for research. *Natural Hazards Review*, **11**(2), pp.69-81.

Mai, P.M. and Beroza, G.C., 2002. A spatial random field model to characterize complexity in earthquake slip. *Journal of Geophysical Research: Solid Earth*, **107**(B11), pp.ESE-10.

Mansinha, L. & Smylie, D., 1971. The displacement fields of inclined faults, *Bulletin of the Seismological Society of America*, **61**(5), 1433–1440.

Melgar, D., LeVeque, R. J., Dreger, D. S., & Allen, R. M., 2016. Kinematic rupture scenarios and synthetic displacement data: An example application to the Cascadia subduction zone, *Journal of Geophysical Research: Solid Earth*, **121**(9), 6658–6674.

Melgar, D., 2021. Was the January 26th, 1700 Cascadia Earthquake Part of an Event Sequence?, *Journal of Geophysical Research: Solid Earth*, [preprint available at https://eartharxiv.org/repository/view/2029/]

Munk, W., Snodgrass, F. and Carrier, G., 1956. Edge waves on the continental shelf. *Science*, **123**(3187), pp.127-132.

Okal, E.A., 1988. Seismic parameters controlling far-field tsunami amplitudes: A review. *Natural Hazards*, **1**(1), pp.67-96.

Park, H., Cox, D.T., Alam, M.S. and Barbosa, A.R., 2017. Probabilistic seismic and tsunami hazard analysis conditioned on a megathrust rupture of the Cascadia Subduction Zone. Frontiers in built environment, 3, p.32.

Peters, R., Jaffe, B., Gelfenbaum, G., & Peterson, C., 2003. Cascadia tsunami deposit database, *US Geological Survey Open-File Report*, pp. 03–13, http://pubs.usgs.gov/of/ 2003/0013/.

Plafker, G., 1997. Catastrophic tsunami generated by submarine slides and back-arc thrusting during the 1992 earthquake on eastern Flores I., Indonesia, *Geol. Soc. Am.*, **29**(57).

Priest, G.R., Goldfinger, C., Wang, K., Witter, R.C., Zhang, Y. and Baptista, A.M., 2010. Confidence levels for tsunami-inundation limits in northern Oregon inferred from a 10,000-year history of great earthquakes at the Cascadia subduction zone. *Natural Hazards*, **54**(1), pp.27-73.

Priest, G.R., Witter, R.C., Zhang, Y.J., Wang, K., Goldfinger, C., Stimely, L.L., English, J.T., Pickner, S.G., Hughes, K.L., Wille, T.E. and Smith, R.L., 2013. Tsunami inundation scenarios for Oregon. Oregon Department of Geology Mineral Industries Open-File Report O-13, 19.

Rabinovich, A. B., 1997. Spectral analysis of tsunami waves: Separation of source and topography effects, *Journal of Geophysical Research: Oceans*, **102**(C6), 12663–12676.

Ramos, M. D., Huang, Y., Ulrich, T., Li, D., Gabriel, A. and Thomas, A., 2021, Assessing margin-wide rupture behavior along the Cascadia megathrust using 3-D dynamic rupture simulations, *Journal of Geophysical Research* [preprint available at https://eartharxiv.org/repository/view/2141/]

Salaree, A. and Okal, E.A., 2020. Effects of bathymetry complexity on tsunami propagation: a spherical harmonics approach. *Geophysical Journal International*, **223**(1), pp.632-647.

Satake, K., 2015. Geological and historical evidence of irregular recurrent earthquakes in Japan. Philosophical Transactions of the Royal Society A: Mathematical, Physical and Engineering Sciences, 373(2053), p.20140375.

Satake, K., Shimazaki, K., Tsuji, Y., & Ueda, K., 1996. Time and size of a giant earthquake in Cascadia inferred from Japanese tsunami records of January 1700, *Nature*, **379**(6562), 246.

Satake, K., Wang, K., & Atwater, B. F., 2003. Fault slip and seismic moment of the 1700 Cascadia earthquake inferred from Japanese tsunami descriptions, *Journal of Geophysical Research: Solid Earth*, **108**(#2535), 17pp.

Schmalzle, G. M., McCaffrey, R., & Creager, K. C., 2014. Central Cascadia subduction zone creep, *Geochemistry, Geophysics, Geosystems*, **15**(4), 1515–1532.

Shuto, N., Suzuki, T., & Hasegawa, K., 1986. A study of numerical techniques on the tsunami propagation and run-up, *Science of Tsunami Hazard*, **4**, 111–124.

Stein, S. and Wysession, M., 2009. *An introduction to seismology, earthquakes, and earth structure.* John Wiley & Sons. Vancouver.

Synolakis, C. E., Bernard, E. N., Titov, V. V., Kânoglu, U., & González, F. I., 2008. Validation and verification of tsunami numerical models, **in:** *Tsunami Science Four Years after the 2004 Indian Ocean Tsunami* (pp. 2197-2228). Birkhäuser Basel.

Thingbaijam, K.K.S., Martin Mai, P. and Goda, K., 2017. New empirical earthquake source−scaling laws. *Bulletin of the Seismological Society of America*, **107**(5), pp.2225-2246.

Thio, H.K. and Somerville, P., 2009. A probabilistic tsunami hazard analysis of California. **In:** *TCLEE 2009: Lifeline Earthquake Engineering in a Multihazard Environment* (pp. 1-12).

Thio, H. K., Somerville, P. and Polet, J., Probabilistic Tsunami Hazard in California, *Pacific Earthquake Engineering Research Center Report, UC Berkeley Publications*, 2010

Titov, V.V. and Synolakis, C.E., 1998. Numerical modeling of tidal wave runup. Journal of Waterway, Port, Coastal, and Ocean Engineering, 124(4), pp.157-171.

Titov, V., Kâno˘glu, U., & Synolakis, C., 2016. Development of MOST for real-time tsunami forecasting, *Journal of Waterway, Port, Coast and Oceanic Engineering*, **142**, 03116004–1–03116004–16.

Wang, K., Wells, R., Mazzotti, S., Hyndman, R.D. and Sagiya, T., 2003. A revised dislocation model of interseismic deformation of the Cascadia subduction zone. *Journal of Geophysical Research: Solid Earth*, **108**(B1).

Wang, K. & Dixon, T., 2004. "coupling" semantics and science in earthquake research, *Eos, Transactions American Geophysical Union*, **85**(18), 180.

Wang, K. & Tréhu, A. M., 2016. Invited review paper: Some outstanding issues in the study of great megathrust earthquakes – The Cascadia example, *Journal of Geodynamics*, **98**, 1–18.

Watt, J.T. and Brothers, D.S., 2021. Systematic characterization of morphotectonic variability along the Cascadia convergent margin: Implications for shallow megathrust behavior and tsunami hazards. *Geosphere*, **17**(1), pp.95-117.

Wessel, P. and Smith, W.H., 1998. New, improved version of Generic Mapping Tools released. *Eos, Transactions American Geophysical Union*, **79**(47), pp.579-579.

Williamson, A., Melgar, D., & Rim, D., 2019. The effect of earthquake kinematics on tsunami propagation, *Journal of Geophysical Research: Solid Earth*. **124**, 11639-11650

Witter, R.C., Zhang, Y., Wang, K., Priest, G.R., Goldfinger, C., Stimely, L.L., English, J.T. and Ferro, P.A., 2011. Simulating tsunami inundation at Bandon, Coos County, Oregon, using hypothetical Cascadia and Alaska earthquake scenarios. *Oregon Department of Geology and Mineral Industries Special Paper*, 43, p.57.